

Analysis of water-in-gasoline emulsions via experiments and direct numerical simulations

Benjamin Blau¹ (✉), Oscar Krzeczek², Christoph Heinrich¹, Markus Klein²

1. Institute of Automotive Technology, Trier University of Applied Sciences, Trier D-54293, Germany

2. Institute of Applied Mathematics and Scientific Computing, University of the Bundeswehr Munich, Neubiberg D-85579, Germany

Abstract

This work explores the combination of direct numerical simulations (DNSs) and experimental approaches for studying technical emulsification processes. Although emulsions have long been used in a variety of industries and many important research papers have been published over the years, quantifying and predicting the dispersion of droplets in another liquid remains challenging because of the complex multiphase nature and microscopic droplet scales. This study focuses on water-in-gasoline emulsions, which have the potential to improve efficiency and reduce emissions in combustion-based power generation. Experimental data from two different emulsion injection systems are complemented with DNS to gain insight into emulsification and the resulting droplet size distribution. In situ shadow imaging is used to acquire the experimental droplet size distributions, whereas DNS is performed via the geometric volume of fluid (VoF) method with the open-source code PARIS. The results indicate consistent agreement between the experimental and simulation results. Additionally, a corresponding trend of increasing droplet size is observed as the volume fraction of the dispersed phase increases. Furthermore, a detailed analysis of various probability density functions for modeling droplet size distributions (DSDs) reveals that the gamma distribution is the most appropriate. Overall, this work demonstrates that DNS can be successfully combined with experiments to increase the understanding of emulsification processes.

Keywords

emulsion
direct numerical simulation (DNS)
multiphase flow
water injection
droplet size distribution (DSD)

Article History

Received: 31 January 2024

Accepted: 4 May 2024

Research Article

© The Author(s) 2025

1 Introduction

Emulsions and other dispersed liquid-liquid multiphase flows have been extensively studied over the years because of their high relevance in the chemical, food, oil and pharmaceutical industries (see, e.g., Angardi et al., 2022; Plasencia et al., 2022; Rayner and Dejmek, 2015; Spornath and Aserin, 2006). The emulsification process can be divided into two substeps. The fragmentation of the droplets of the dispersed phase and subsequent stabilization by emulsifying agents prevent coalescence and segregation. Energy input from the flow field is required for droplet breakup. These disintegrating forces compete with the interfacial tension forces and the viscosity forces of a drop. If the former predominates, the droplet is deformed and, depending on the level and duration of the stress, ultimately breaks up.

This is a very complex process due to various influencing factors from both phases and the flow field, which, in most technical applications, is three-dimensional and turbulent.

Many studies have been conducted to understand the basic principles of droplet breakup in turbulent flows. They are often based on a formulation of a critical Weber number in conjunction with the empirical correlations proposed by Hinze (1955) to calculate the maximum stable droplet diameter, which cannot be broken up by turbulence. The forces relevant for droplet breakup in homogeneous isotropic turbulence (HIT) are defined as the mean squared velocity difference at a distance equal to the droplet diameter. Several studies have been published that discuss and extend the basic Hinze model (Crales-Esposito et al., 2023; Hesketh et al., 1987; Krzeczek et al., 2023; Sleicher, 1962).

✉ blaub@hochschule-trier.de

In recent years, the ever-increasing capability of computational power has led to various numerical studies on this topic. Many publications have focused on the behavior of emulsions in response to varying physical parameters via direct numerical simulations (DNSs). For example, numerical methods have been employed to investigate the influence of the volume fraction on the breakup and coalescence processes of emulsions (Crialesi-Esposito et al., 2022; Mukherjee et al., 2019). For example, Perlekar et al. (2012) reported good agreement with the Hinze model at low dispersed phase volume fractions via their simulation. Further numerical work concerns the change in material parameters or the impact of varying flow dynamics, represented by Weber and Reynolds numbers. Begemann et al. (2022) investigated the influence of the turbulence intensity and surface tension on emulsions with the forcing method used in this work. On this basis, Krzeczek et al. (2023) investigated the influence of the density ratio on turbulent emulsions, confirmed and extended the formulation of the Hinze model derived by Hesketh et al. (1987), and supplemented the analyses of the segregation process by Trummler et al. (2022).

Moreover, efforts have been made to compare numerical findings with experimental results to better understand droplet breakup. Håkansson et al. (2022) compared numerical and experimental results and characterized the critically deformed state of small viscous drops during turbulent breakup in emulsification processes. Olad et al. (2023) compared droplet breakup in two different settings, homogeneous and isotropic flow, and a simplified high-pressure homogenizer through numerical experiments. They reported correlations between the breakup time and the Weber number and summarized similarities and differences between experiments and numerical analyses. In previous works, Deberne et al. (2024) numerically analyzed droplet breakup under turbulent flow with moderate Reynolds and Weber numbers. The study confirmed a four-stage breakup process and described the final stages of this process with shape parameters, matching the previous findings of both experimental and numerical investigations.

With respect to technical applications, work has focused mainly on emulsification in high-pressure homogenizers (Stang et al., 2001) or stirred vessels (Maaß et al., 2012). Since emulsifiers are mandatory for long-term stability, little effort has been made to investigate nonstabilized emulsions. However, some related work has been published on dispersed water-oil pipe flow without the use of surface active agents (Galinat et al., 2007; Schümann et al., 2016). For example, Angeli and Hewitt (2000) carried out droplet size distribution measurements in a pipe, investigating the influence of the pipe material and correlating the results

with the Hinze model and extensions of it.

The work presented here focuses on nonstabilized water-in-gasoline emulsions. They are promising technologies that can help achieve CO₂ neutrality and minimize pollutant emissions for combustion-based transportation. The main mechanism behind this possibility is internal cooling of the engine by the evaporation of water. Owing to the lower temperature of the cylinder charge at the end of the compression stroke, the tendency of abnormal combustion events, known as “engine knock”, which can damage the engine, can be avoided. Combustion phasing can be advanced toward the point of maximum efficiency, exhaust gas temperatures are thereby reduced, and the injection of surplus fuel (rich air-fuel mixture) to avoid temperature-related damage to components in the exhaust system is no longer needed. Moreover, pollutant emissions are also positively affected by the addition of water (Akehurst et al., 2019; Gern, 2021; Rohit et al., 2017). The use of emulsions to introduce water to the combustion process is not new. Peters and Stebar (1976) investigated the influence of this phenomenon in the 1970s by feeding stabilized water-in-gasoline emulsions with up to 40% water to a test engine. They identified positive influences on the emission behavior and the knock limit of the engine but also reported that the emulsifier used has a negative effect on those parameters.

Gasoline-water direct injection (GWDI) is the approach followed in this work, which is different since the emulsion is produced directly in the injection system of the engine. This makes it possible to dispense with the use of emulsifiers. Although the thermodynamic potential of this concept has been proven (Durst et al., 2017; Heinrich et al., 2018; Hermann et al., 2018), many unanswered questions remain regarding such emulsions. The quality of emulsions produced in GWDI systems affects the subsequent atomization process and, ultimately, engine operation. Therefore, it is necessary to quantify emulsion formation, emulsion properties, and emulsion stability. Only a few studies address this topic. Sazonov et al. (2019) conducted qualitative analyses to obtain information about the segregation behavior and the influence of ethanol in the fuel on the emulsion. Problems during engine operation with GWDI were identified by Hermann et al. (2017). An optimized injection system design to prevent segregation and optimize the system response under transient operation was proposed by Durst et al. (2017).

In our study, water-in-gasoline emulsions were quantified on the basis of the droplet size of the dispersed phase, which is the most important quality parameter of emulsions. To examine this experimentally, different techniques have been developed. Often, laser-based methods, such as laser diffraction or laser back-scattering, are used (Maaß and Kraume, 2012; Simmons, 2000). Moreover, microscopic

imaging techniques are often applied (Boxall et al., 2010). However, these methods are limited by the opaque emulsion appearance at technically relevant dispersed phase volume fractions. Therefore, sampling and dilution are often mandatory steps. In our case, this is not possible because of the nonstabilized emulsion, which needs to be quantified directly in the injection system to avoid unwanted segregation influences.

From a simulation point of view, it is also a very challenging task to model droplet breakup behavior and resolve single droplets. DNSs that require high computational effort are able to resolve the turbulence spectra responsible for droplet breakup. However, these simulations are limited to simplified geometries owing to the high number of cells required and to idealized flow conditions such as HIT.

On the basis of the previous explanations, experiments and simulations are clearly limited by various factors. The main goal of this study is, therefore, to compensate for these effects by combining DNS and experiments to obtain a deeper understanding of the emulsification process and the resulting properties of water-in-gasoline emulsions. This includes qualitative analysis of the droplet shape and quantitative analysis of the droplet size distributions. Moreover, we investigate the possibility of describing these distributions with various probability distribution functions found in the literature.

2 Experimental setup

Experiments were conducted on an injection system test bench specially developed for emulsion investigations. In the following, the two prototype injection systems are described, and the experimental methodology is discussed.

2.1 Injection systems

Schematic illustrations of both GWDI systems are presented in Fig. 1. The systems are shown in a four-cylinder layout because engine testing is conducted on a four-cylinder engine. Standard gasoline direct-injection components are used for simplicity: a low-pressure fuel-feeding system, a high-pressure fuel pump, a common rail for damping pressure oscillations and fuel injectors. Typically, emulsions are stabilized by surfactants, which can increase the lifetime of emulsified products for months or years. For GWDI, no emulsifiers are used because of the low temporal stability required and the negative influences of some surfactants, such as deteriorating engine combustion (Heinrich et al., 2017; Peters and Stebar, 1976).

The single-high-pressure pump (Single-HPP) concept is a rather simple setup without any major modifications to the high-pressure part of the system. A single mixing

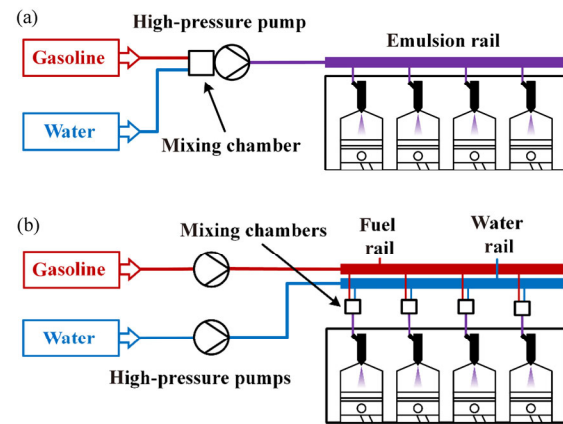


Fig. 1 Simplified illustration of both GWDI systems: (a) single-HPP system and (b) on-injector system. The red color denotes gasoline, the blue color denotes water, and the purple color denotes emulsion.

chamber upstream of the high-pressure pump is responsible for the water admixture. Water is injected into the fuel flow by an injection valve normally used for gasoline. Its opening period controls the water volume fraction. Emulsification has been demonstrated to be a two-stage process (Blau et al., 2022). First, a coarse emulsion is produced by jet disintegration of the water in the mixing chamber. Then, further droplet fragmentation occurs in the single-piston high-pressure pump, probably at the inlet and outlet valves of the pump cylinder, where high flow velocities and, most likely, increased turbulence are present. Similar concepts have already been proposed in the literature (Durst et al., 2017; Hermann et al., 2017).

The on-injector system, on the other hand, is a more sophisticated approach. The goal was to introduce water as close as possible to the emulsion injectors to minimize dead times and to ensure that each engine cylinder received the right amount of water. The system is composed of two high-pressure systems, one for gasoline and one for water. The emulsion is produced in mixing chambers upstream of the injectors, separately for each engine cylinder. The water is injected into the gasoline flow at a 50 bar higher pressure level. Like in the single-HPP approach, the opening duration of the water valves controls the water volume fraction. Droplet break-up is based primarily on the disintegration of water jets in gasoline.

The main differences between the two approaches are the system complexity, the type and place of emulsification, and the size of the emulsion-filled volume. Therefore, the emulsion properties are expected to vary between the systems.

2.2 Experimental methods

There are different measurement methods available for

analyzing the droplet size distribution in dispersed liquid/liquid systems. These methods often involve taking samples and diluting them, especially when certain optical methods are employed. However, such techniques are not suitable for this purpose because of the low temporal stability of nonstabilized water-in-gasoline emulsions. Therefore, an in situ measurement setup was developed, comprising a shadowgraph imaging system and a flow-cell for optical access to the high-pressure injection system. The cell is designed for pressures up to 200 bar, corresponding to the maximum system operating pressure. It consists of a steel cage and special borosilicate glass windows. The optically accessible flow cross section is rectangular. The channel is 0.5 mm deep along the optical axis to achieve the most efficient illumination of the flow. Bypasses above and below the channel defined by the glass windows expand the flow cross-section overall to similar values as the piping from the rail to the injectors, in which the cell is integrated. The shadow imaging system from LaVision consists of three main components: an illumination unit on one side of the flow cell, a camera with a far-field microscope on the opposite side and a control unit. The Imager CX-5 camera has five megapixels and a maximum frame rate of 83 Hz at 12 bits. An Infinity K2 Distamax far-field microscope with a CF2 objective attached to the camera allows a magnification of 2.7–1.5 at working distances from 140 to 200 mm. An LED flashlight Inspex with a minimum pulse duration of 100 ns is used for illumination. The camera and the light sources are triggered by the PTU X control unit. The operating parameters are set on the PC within the DaVis 10.2 software from LaVision.

Droplet detection and sizing are performed via the

ParticleMaster Shadow software package within DaVis. The droplets are detected via image segmentation. First, the raw images are normalized and then binarized. Filters can be applied to adjust the detection characteristics. These settings were iteratively adjusted to achieve optimal droplet detection for the emulsion images. The parameters must remain constant across all measurement points, as any adjustment could bias the resulting size distributions and render comparisons invalid. After detection, the diameter of a drop is calculated on the basis of the corresponding area in the image under the assumption of a spherical shape. This method does not produce a significant error since the emulsion droplets all exhibit a virtually spherical shape, as shown in Fig. 5(a). For volume distributions, the droplet volume is calculated from its diameter. The size distributions were determined on the basis of 150 individual images per measuring point. This represents a good compromise between a low statistical deviation of the measured values and data manageability.

For emulsion investigations, an injection system test bench was developed, enabling operation independent of the combustion engine. The test bench is integrated into the laboratory's own fuel supply system. At the gravimetric fuel scale, gasoline flows into the test bench's fuel supply system, which consists of a pump, a pressure regulator, and a filter. The water supply is ensured by a storage tank next to the test rig. From there, the water flows via a gravimetric scale to determine the mass flow into the supply system, which is equipped with the same components as the fuel system. Figure 2 provides an overview of the on-injector test layout. The high-pressure pumps are driven by an electric motor. The water is pumped with a flow-controlled

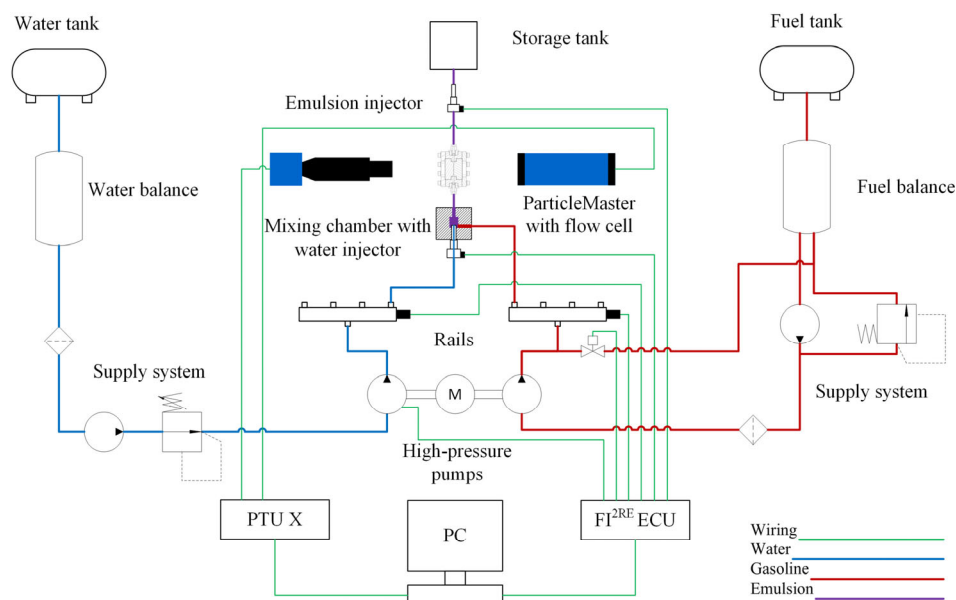


Fig. 2 Test bench layout in the on-injector configuration.

pump. The fuel is brought to the injection pressure level via a two-piston pump with an external pressure control valve. The test bench is equipped with various temperature and pressure sensors for monitoring and ensuring constant conditions. On the test bench, a single-cylinder configuration is implemented, as a multicylinder setup is not required for the current investigations. The flow-cell is implemented downstream from the mixing chamber immediately after emulsification, which is the final state before atomization by the emulsion injector.

The injection systems are controlled by a rapid-prototyping engine control unit. The test cases were chosen to represent engine operating points relevant to water injection. The injection frequency was set to 25 Hz, which corresponds to an engine speed of 3000 r/min. The fuel flow rate was fixed, and the water flow rate was adjusted to achieve the desired dispersed phase volume fraction. The fuel system pressure set point was 150 bar.

3 Computational method and procedure of the simulation

The simulations are conducted via the open-source code PARIS (PARallel, Robust, Interface Simulator) (Aniszewski et al., 2021), which uses the one-fluid formulation of the incompressible Navier–Stokes equations. The continuity and momentum equations can be written as

$$\frac{\partial \mathbf{u}_i}{\partial x_i} = 0 \quad (1)$$

$$\rho \left(\frac{\partial \mathbf{u}_i}{\partial t} + \frac{\partial \mathbf{u}_i \mathbf{u}_j}{\partial x_j} \right) = -\frac{\partial p}{\partial x_i} + \frac{\partial}{\partial x_j} \left[\mu \left(\frac{\partial \mathbf{u}_i}{\partial x_j} + \frac{\partial \mathbf{u}_j}{\partial x_i} \right) \right] + \gamma n_i \kappa \delta_s + \rho \mathbf{g}_i \quad (2)$$

Here, μ denotes the dynamic viscosity, p the pressure, ρ the density, \mathbf{u} the velocity vector, γ the interfacial tension coefficient between the carrier and dispersed fluid, and \mathbf{g} the gravitational acceleration vector. In each computational cell, density and viscosity are linearly interpolated via the

local volume fraction α of the dispersed phase, which is determined via the geometrical volume-of-fluid (VoF) method. The surface tension force is calculated by employing the continuous surface force (CSF) approach of Brackbill et al. (1992), which is computed with an advanced height function technique by Popinet (2009). The VoF marker function is performed via a geometric interface reconstruction algorithm. Spatial discretization is achieved with a cubic, equidistant grid. The Poisson equation for pressure is solved via the projection method with overrelaxation (SOR). Temporal derivatives are calculated via a second-order predictor–corrector approach. The convective term in the momentum equation is approximated by the third-order quadratic upstream interpolation for convective kinematics (QUICK) scheme, whereas the viscous term is discretized via second-order central differences.

First, using a modified linear forcing method by Begemann et al. (2022), a statistically steady state is created for the carrier phase. Then, the dispersed phase is initialized in the form of droplets. Further forcing generates a homogeneous isotropic state (HIT) of the emulsion. The DNS procedure is illustrated in Fig. 3.

3.1 Method for droplet detection

A central role in this work is to evaluate the droplet size distributions. An algorithm proposed by Chan et al. (2021) is used to detect droplets in the VoF field. The threshold value, which indicates how large the volume fraction in a cell must be to be assigned to the dispersed phase, is set to 0.1 since this value is suggested to be the best for our configurations (cf., Chan et al., 2021). The droplet diameter is calculated on the basis of volume while assuming sphericity. The smallest occurring diameter in the statistical distribution of droplets is determined via the criterion suggested by Ling et al. (2015), which is defined as $d_{\min} = 4L/N$. Droplets with diameters smaller than d_{\min} are not resolved well enough by the VoF method, as mentioned in Ling et al. (2015), Mukundan et al. (2021)

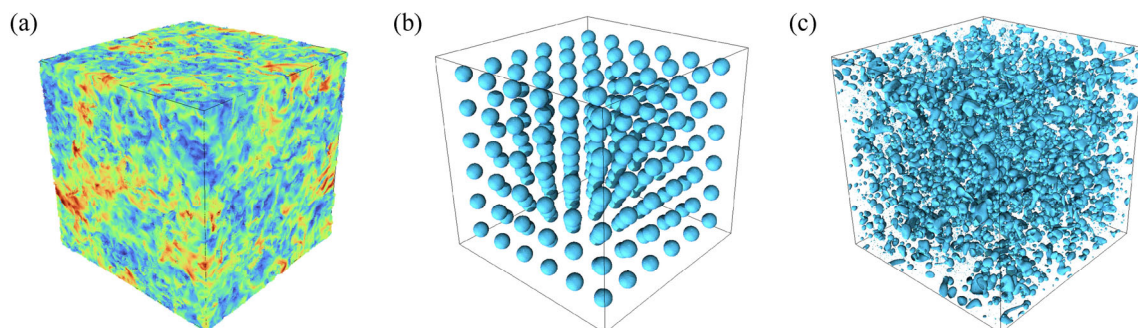


Fig. 3 Simulation setup: (a) single-phase forcing, (b) initialization of the droplets of the disperse phase, (c) turbulent emulsion in the statistically steady state.

and Trautner et al. (2023). Notably, the resolution in this work was high enough to select and resolve all the droplets. Thus, no drops were removed.

4 Comparability of the simulation and experiment results

The fluid parameters of the experiment were measured, and the DNS values were adjusted accordingly to ensure similar conditions. Additionally, the degree of turbulence and the forces acting on the droplets must be comparable. However, owing to the complex flow conditions in the mixing chamber of the on-injector system and the high-pressure pump in the single-HPP system, where droplet fragmentation and emulsion formation occur, the pipe flow upstream of one of the emulsion injectors, where the flow-cell is located, was taken as a reference. These flow conditions are virtually identical for both injection systems. Owing to the periodic opening and closing of the injector, the pipe flow is unsteady. On the basis of the flow rate of the emulsion injector, a mean flow velocity of 2.8 m/s in a circular pipe with a diameter of 3 mm can be estimated when the injector is open and the flow is established.

To describe the deformation and break-up of the droplets, we consider the Hinze scale d_H . It is defined as the diameter of the smallest stable bubble or droplet that can withstand the forces applied by the surrounding flow field in homogeneous isotropic turbulence; see Hinze (1955). Hesketh et al. (1987) derived Eq. (3) for liquid-liquid dispersions in horizontal pipelines, which was also proven to be accurate for a similar numerical case by Krzeczek et al. (2023):

$$d_H = \left(\frac{We_{d,crit}}{2} \right)^{3/5} \left(\frac{\rho_c}{\gamma} \right)^{-3/5} \epsilon^{-2/5} \left(\frac{\rho_d}{\rho_c} \right)^{-1/5} \quad (3)$$

where ϵ is the dissipation rate, ρ_c the density of the carrier phase, γ the interfacial tension between water and gasoline, and $We_{d,crit}$ the critical Weber number, which is assumed to be 1.17 following Hinze (1955). This number was confirmed in previous numerical work (Perlekar et al., 2012) and experimental studies (Yi et al., 2021).

To define an experimental Hinze scale, the dissipation rate is evaluated via the formula given in Hesketh et al. (1987):

$$\epsilon = \bar{\epsilon} = \frac{2fv^3}{D} \quad (4)$$

where D is the pipe diameter. $f = 0.079/Re_c^{0.25}$ denotes the friction factor, assumed to be represented by the Blasius relation, as in Hesketh et al. (1987). Re_c is the carrier-phase Reynolds number.

To compare the degree of turbulence, we use the turbulent Reynolds number, which can be expressed as

$$Re_t = \frac{L_t u'}{\nu_c} \quad (5)$$

where L_t is the integral length scale, u' is the velocity fluctuation, and ν_c is the kinematic viscosity of the carrier phase. Re_t describes the ratio of inertial to viscous forces and provides information on the degree of turbulence of the emulsion. For the experimental value, the velocity fluctuation u' is assumed to be ten percent of the mean velocity, and the turbulent length scale is assumed to be 1/4 of the pipe diameter. The turbulent Ohnesorge number is also presented, which relates the viscous forces to the inertial and surface tension forces

$$Oh_t = \frac{\mu_d}{\sqrt{\rho_d \gamma L_t}} \quad (6)$$

where μ_d is the dynamic viscosity of the disperse phase, ρ_d the density of the disperse phase, γ the interfacial tension between gasoline and water, and L_t the turbulent length scale.

The constant parameters for DNS and the experiment are compared in Table 1. To ensure comparability, the Hinze scales d_H were normalized using the length S , which represents the pipe diameter in the experiment and the domain length in the simulation. Standard gasoline with an ethanol content of 5.6% and deionized water were used for the experiments, and the relevant fluid properties ρ , η , and γ were measured. All the turbulent quantities in Table 1 are higher for the simulation but still at the same order of magnitude. These differences arise from the many assumptions that must be made to quantify the experimental conditions.

The turbulent kinetic energy (TKE) in the DNS is set to $k = 0.5 \text{ m}^2/\text{s}^2$, which creates turbulent conditions comparable to those of the turbulent pipe flow in the experiment. The influence of the TKE on the DSDs is shown in Fig. 12 and discussed in the Appendix. Following Rosales and Meneveau (2005), the integral length scale is $L_t = 0.2L$, where $L = 2\pi \text{ m}$ is the domain size. A square domain with periodic boundary conditions was employed to generate the turbulent emulsion. The dissipation rate is $\epsilon = 0.153 \text{ m}^2/\text{s}^3$. The grid resolution was determined on the basis of the criterion $N \geq 1.5L / (\pi\eta_K)$ (Pope, 2001), where

Table 1 Physical parameters of the experiment and DNS

	γ (N/m)	ν_d/ν_c	ρ_d/ρ_c	Re_t	Oh_t	d_H/S
DNS	0.027	2.28	1.34	726	14.3×10^{-3}	0.026
Experiment	0.027	2.28	1.34	484	7.0×10^{-3}	0.078

η_k represents the Kolmogorov microscale and $N = 1024$ denotes the cell count in one direction.

We compare the droplet size distributions at two different water volume fractions, $\phi = 2.6\%$ and $\phi = 5.3\%$.

$$\phi = \frac{V_d}{V_d + V_c} \quad (7)$$

5 Results and discussion

In this section, the results of this study are discussed. First, some details of the experimental findings are presented, followed by a comparison with the numerical data and an analysis of the statistical distribution functions for describing the volume distributions.

5.1 Injection system comparison

As mentioned in Section 2.1, the emulsification process is different in both injection systems. The main motivation behind the experimental work generally lies in identifying influences on the emulsion droplet size and understanding any differences arising from the system layout. A summary of the experimental findings is given here. Supplementary insight can be found in Blau et al. (2023).

Figure 4 shows the volume size distributions at different water volume fractions for both GWDI systems. The emulsion was measured upstream of the emulsion injector. This point differs in both systems regarding the time the emulsion has spent in the injection system. The period is significantly greater in the single-HPP system. After the droplet breakup in the high-pressure pump, the measurements show that the droplet size actually increases due to coalescence, most likely occurring in the emulsion rail. This can be explained by the comparatively low flow velocities and high residence times in this component, which promote emulsion segregation. In the on-injector system, on the

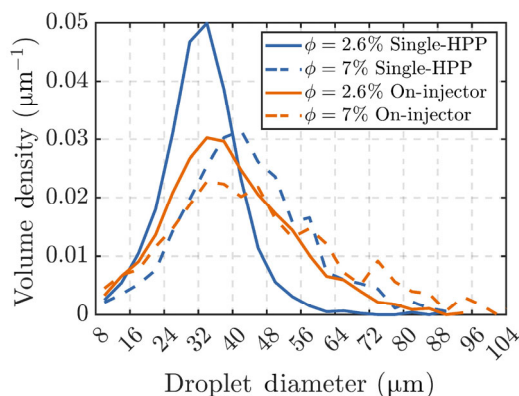


Fig. 4 Comparison of volume density distributions at water volume fractions of 2.6% and 7% between the single-HPP system and the on-injector system at 150 bar system pressure.

other hand, droplet breakup has just taken place upstream of the measuring point in the mixing chamber. Here, any segregation processes are assumed to be less dominant because of the shorter time scale.

The resulting droplet size distributions are plotted in Fig. 4. A comparison of the two systems at a dispersed phase volume fraction of 2.6% indicates a narrower distribution for the single-HPP approach, with a higher peak at 34 μm . The distribution of the on-injector system also peaks at 34 μm but has a much smaller amplitude. Moreover, the spread of the distribution is larger, with a larger fraction at droplet diameters above 42 μm . This finding indicates that emulsification in the on-injector system leads to larger droplets. At a volume fraction of 7%, both distributions are shifted toward larger diameters, and they have a wider spread. Comparing the two systems, the single-HPP distribution is narrower, with a higher peak at 42 μm . However, overall, the differences between the distributions are smaller than those at low volume fractions.

These results indicate that the distributions are shifted to smaller droplet diameters in the single-HPP system than in the on-injector approach despite the segregation occurring after emulsification. This is because the droplet breakup in the high-pressure pump is more intense than the jet disintegration of the water in the mixing chamber of the on-injector system. In fact, the droplets are initially so small that this compensates for the segregation in the rail, and the resulting droplets are still smaller.

An overall increase in droplet size with increasing water volume fraction was observed in both systems throughout the investigated range. This can be explained by an increased coalescence rate. A higher dispersed phase volume fraction is associated with an overall increased droplet quantity. More droplets collide and ultimately converge due to the nonstabilized interface.

Summarizing all the insights based on the experimental emulsion analysis, it can be concluded that the emulsion in the injection system is influenced not only by the system design and the water volume fraction but also by operating parameters such as pressure and flow rate (Blau et al., 2022, 2023). The observed differences between the two systems are relatively small in terms of the absolute droplet size. Whether these factors influence the emulsion spray properties is currently being investigated via experimental spray droplet size analysis.

5.2 Comparison of the numerical and experimental results

In this section, the experimental and numerical results are compared. First, an introductory comparison is made on the basis of the Sauter mean diameter (SMD) and the

Ohnesorge number $Oh_{d_{32}}$ calculated with the SMD as a representative droplet size to relate the fluid properties to the results.

The Sauter mean diameter describes a mean droplet size with the same volume-to-surface ratio as the sum of all droplets and is defined by Eq. (8):

$$d_{32} = \frac{\sum_{i=1}^N n_i d_i^3}{\sum_{i=1}^N n_i d_i^2} = \frac{6V_d}{A} \quad (8)$$

where V_d represents the dispersed phase volume and A the surface area between the dispersed and continuous phases.

In Table 2, the Ohnesorge number and d_{32} values are shown. Here, the Sauter mean diameter is normalized by the length S to address the different size scales in the experiment and simulation. A comparison of the experimental and simulation values indicates that the droplets are significantly larger in proportion to the domain length and, accordingly, the pipe diameter in the experiment. However, the SMD increases in the same proportion as the dispersed phase volume fraction increases in all investigated cases. This implies that the DNS shows the same behavior regarding coalescence because the dispersed volume fraction increases. If one compares the SMD with the Hinze scale in Table 1, the value for the DNS is clearly smaller than the resulting Sauter mean diameters. This implies that the normalized d_H does not predict the maximum stable diameter for the simulation case since it lies within the distribution. This is often observed in numerical studies (e.g., Cialesi-Esposito et al., 2022; Mukherjee et al., 2019). On the other hand, the experimental Hinze scale is much greater than the resulting Sauter mean diameter and is approximately twice as large as the largest droplets detected. This is an indication that the turbulence in the pipe is not strong enough to further break the droplets. More insight into this is given in Section 5.2.1, where the droplet shape is also taken into account. The resulting Ohnesorge numbers in Table 2 are very similar for the experiments and the DNS, which indicates that the influence of the fluid parameters on the droplet size is concordant. In combination with the details

Table 2 Comparison of the investigated configurations and the resulting Oh and d_{32} values

System	ϕ	$Oh_{d_{32}}$	d_{32} / S
DNS	2.6%	0.036	0.032
	5.3%	0.033	0.038
On-injector	2.6%	0.033	0.011
	5.3%	0.032	0.012
Single-HPP	2.6%	0.035	0.010
	5.3%	0.033	0.012

in Section 4, the turbulence levels responsible for droplet breakup in the simulation and experiment are roughly comparable.

5.2.1 Sectional images

Considering that experimental images of the emulsion are available and that VoF-field images can be extracted from the simulation, a visual comparison is conducted. The experimental image was taken in the on-injector system downstream of the mixing chamber. The experimental limiting factors are the optical density and the depth of field of the long-distance microscope. To compensate for the differing size scales, the images are normalized via the d_{32} . The depth of field of the VoF-image is adjusted to match the experimental depth. This ensures good comparability between the experimental and simulation images.

A qualitative comparison of the images in Fig. 5 indicates strong concordance regarding the droplet density and spatial distribution. Three-dimensional images of the simulation cases can be found in the appendix in Fig. 12. The range of droplet sizes is also consistent. However, the shapes of the larger droplets differ significantly. The droplets in the experimental flow cell all appear to be spherical, whereas in the DNS image, the droplets are partially deformed. The larger the droplets are, the greater the magnitude of deformation. Small droplets look lenticular, but some of the largest droplets have the shape of a dumbbell, which indicates that they may soon break up.

An explanation for this divergent behavior could be the different degrees of stress acting on the droplets at the image recording points. The flow cell in the experiment is positioned downstream of the mixing chamber in the on-injector system. Therefore, the droplet breakup cannot be captured, only its result. Additionally, the spherical shape of the droplets suggests that they are not substantially influenced by the flow field. Additionally, the very high Hinze scale confirms this theory. In the case of the DNS, the image is captured in the controlled HIT environment after reaching a steady state, where the interface between the phases remains constant. This is shown in Fig. 11 in the appendix. This observation implies that the interfacial area between the phases reaches equilibrium and that the breakup and coalescence processes occurring in the simulation must balance each other. Droplets that exceed a critical size due to coalescence become deformed and are eventually fragmented again by the turbulent flow field.

5.2.2 Comparison of droplet size distributions

Since the size scale is different between the DNS and the experiments, establishing a basis for comparison becomes essential. For the droplet size distributions, this is achieved

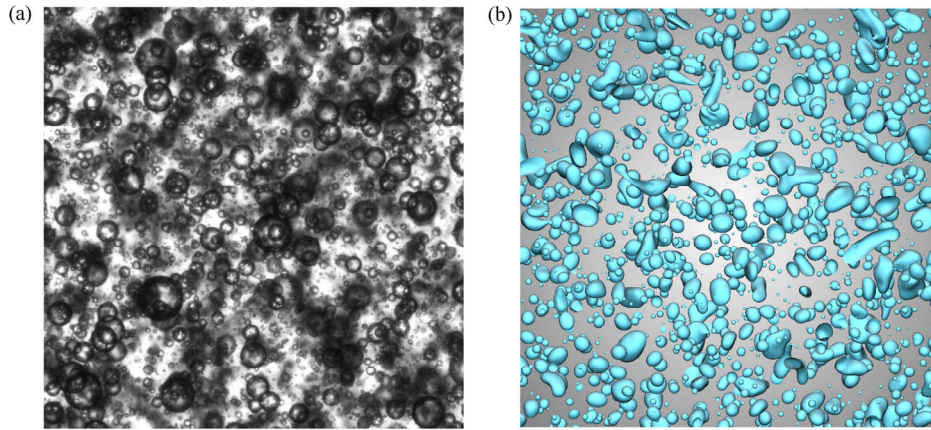


Fig. 5 Comparison of the on-injector shadow image (a) and sectional image from the DNS (b), with a scale of $25 \times d_{32}$ and a depth of field of approximately $10 \times d_{32}$. The dispersed phase volume fraction is 5.3%.

by plotting the relative quantities per size class on the ordinate and a normalized droplet diameter on the abscissa. This normalization is conducted by dividing the droplet size by the Sauter mean diameter d_{32} . In Fig. 6, the number size distributions are plotted for both volume fractions. It is evident that the distributions of the simulation always start at smaller normalized droplet diameters because of the higher droplet detection resolution. Additionally, in the experiment, very small droplets can be identified in the raw images that unfortunately cannot be detected by the software. In Figs. 6(a) and 6(b), comparisons with the on-injector system are plotted. Good agreement can be seen for both volume fractions. The experimental distributions have slightly greater numbers at the start of the curves in the area

of small droplet diameters, but the numerical distributions approach the experimental curves quite well afterwards. At the largest droplet diameters, the differences increase again. In this range, the numerical distributions tend to underestimate the experimental quantities, and the experimental curves extend to larger diameters than the numerical curves do. At a volume fraction of 5.3%, the concordance is stronger.

As already shown in Section 5.1, there are differences between the on-injector and the single-HPP systems. Therefore, it is not surprising that the agreement with the DNS results is less good. At the 2.6% volume fraction, the experimental curve exceeds the simulation curve immediately from the start at small diameters. The high-volume fraction

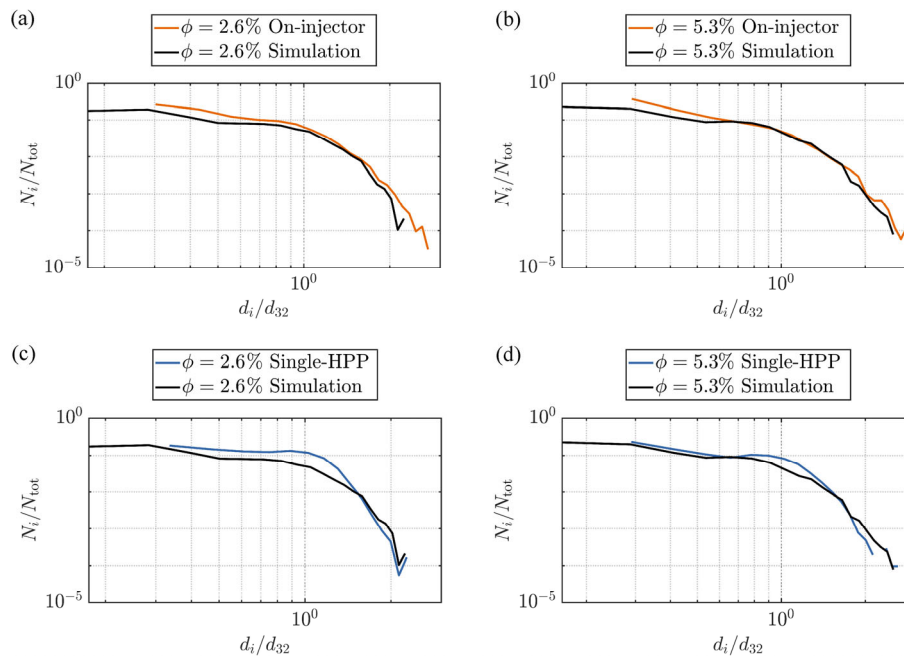


Fig. 6 Number size distribution comparison between DNS and the on-injector system (a, b) and the single-HPP system (c, d).

case, on the other hand, shows very strong concordance at small droplet sizes. For both volume fractions, the experimental distributions exhibit a dent in the middle range, where the normalized droplet diameter is approximately one. At the largest diameters, the agreement is good for the low-volume fraction case. At a volume fraction of 5.3%, the concordance is less pronounced, as the DNS distribution declines more rapidly and steeply.

Droplet size distributions can also be described by volume size distributions. This approach is often adopted when the measuring technique directly measures the volume of droplets per size class instead of merely counting them. In this context, volume distributions are preferred, as the droplet volume plays a more significant role in the vaporization process following injection into the combustion chamber. A comparison between the experimental and DNS results is given in Fig. 7. Like for the number distributions, the DNS accurately predicts the on-injector distributions at both volume fractions. In both scenarios, the height, position of the peak, and width of the distributions show concordance. At a volume fraction of 2.6%, the numerical distribution slightly underestimates the width of the peak. The opposite is the case at 5.3%, as the numerical peak is wider with a small dent around the center. The differences already identified before between the DNS and the single-HPP experiments are highlighted by the volume distribution plots. At both volume fractions, the experimental maximum is significantly greater, and the width of the distributions is narrower. However, the position of the peak is in concordance with that of the DNS.

Considering the simplifications made in the DNS, good agreement is achieved with the on-injector experiments. This finding indicates that the droplet breakup in the mixing chamber in this system can be successfully described via the idealized homogeneous isotropic turbulence approach and that the chosen flow conditions are representative of the experimental conditions.

Obviously, the DNS and single-HPP experiments do not correlate well. The different breakup and coalescence behaviors compared with those of the on-injector approach, as already discussed in Section 5.1, seem to be the reason for those discrepancies. The turbulence levels assumed for the single-HPP system are not representative of the breakup in the pump or the coalescence in the rail downstream.

With respect to the influence of the dispersed phase, the same trend is observed in the simulation as in the experiments. An increase in the dispersed phase also increases the droplet size, indicating that the DNS can predict the coalescence behavior accurately. In all the experimental and numerical distributions, the Sauter mean diameter is close to the droplet size at which the distribution peaks. Therefore, it can be used here as an indicator of the droplet size that possesses the highest proportion of the dispersed phase's volume.

5.3 Fitting probability density functions

In this section, statistical distribution functions are used to further analyze the volume size distributions acquired from experiments and simulations. This approach has the ability

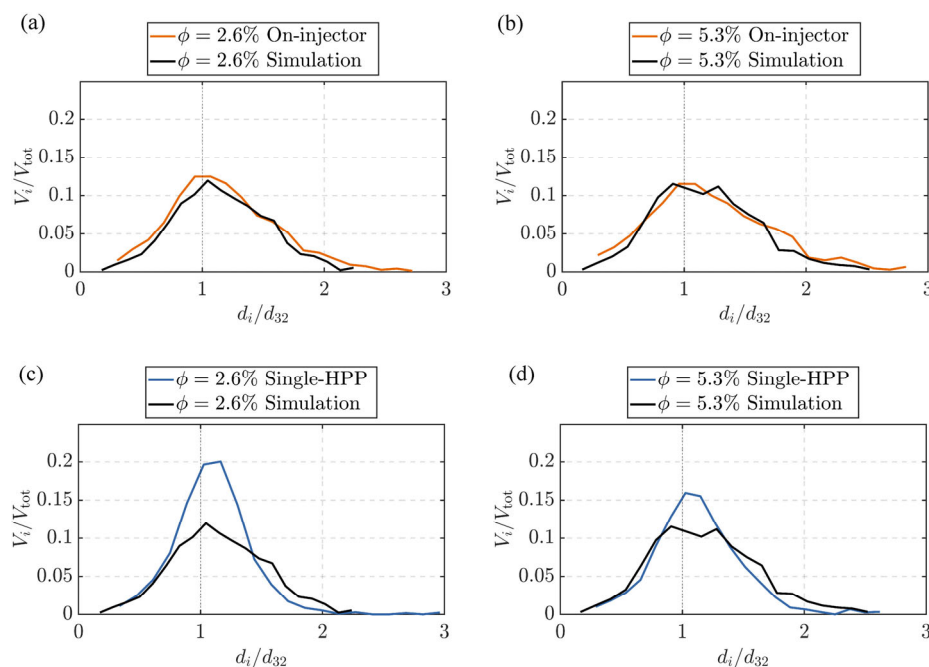


Fig. 7 Comparison of volume distributions between the DNS and the on-injector system (a, b) and the single-HPP system (c, d).

to describe distributions with only a few parameters that define the function. The goal is to predict DSDs for practical applications by using a measurable characteristic diameter and finding empirical values or regularities for the fitting parameters.

Many experimental and numerical publications discuss the application of such functions for the determination of droplet size distributions. Babinsky and Sojka (2002) proposed several statistical distribution functions to describe droplet size distributions. Yi et al. (2021) explored turbulent emulsions by employing the multicomponent Lattice-Boltzmann method. They recommended describing DSDs with a log-normal distribution, which implies that a fragmentation process is the primary mechanism for droplet formation. Furthermore, while they found a Gamma distribution to be suitable, they did not conduct a quantitative analysis of its differences compared with the log-normal distribution. Perlekar et al. (2012) used DNS with a pseudo potential Lattice-Boltzmann method focusing on configurations with different volume fractions and proposed a statistical description with a log-normal function. With a similar numerical method, Skartlien et al. (2013) analyzed log-normal distributions and a Gaussian distribution for droplet sizes in water-oil emulsions. They observed that the distribution shape deviates from the log-normal distribution, especially in the sub-Hinze region. Here, the Gaussian distribution covers this range better. These studies show that most analyses focus on log-normal distributions. However, deviations are frequently observed, particularly at the beginning of the distribution involving small diameters and across various configurations, such as those involving changes in the volume fraction. Additionally, a need persists to compare various statistical distributions of DSDs quantitatively and determine the most accurate functions for their description. Additionally, values for the fitting parameters must be determined to be able to use distribution functions for predicting DSDs in practical applications.

A variety of distribution functions typical for the description of droplets or bubbles in isotropic turbulence or in sprays and emulsions are investigated, and the dependency of the fitting parameters on the different configurations is analyzed. In addition, the distributions are partially modified so that the number of fitting parameters is reduced as much as possible. Only the results for a volume fraction of 5.3% are shown here, but those of the lower volume fraction are very similar. The calculated fitting parameters are listed in Table 4. The single-HPP distributions were not analyzed because this setup apparently deviates more strongly from the idealized HIT DNS configuration. All the equations presented here are given mathematically in the form of density distribution functions. Since this

involves a length scale, the distribution plots are normalized for comparability, as described in Section 5.2.

The log-normal (LN) distribution is commonly used to model the volume distribution of droplets or particles in various scientific and engineering applications (Babinsky and Sojka, 2002; Moradi et al., 2011; Pacek et al., 1998; Panão, 2023; Skartlien et al., 2013; Yi et al., 2021). It is defined by

$$f_{\text{LN}}(d) = \frac{1}{\sqrt{2\pi}\sigma d} \exp\left(-\frac{1}{2}\left(\frac{\ln(d/\mu)}{\sigma}\right)^2\right) \quad (9)$$

where d represents the detected droplet diameter, μ the mean value of the distribution, and σ the width of the distribution used as a fitting parameter. μ corresponds to $d_{50,3}$, the median volume droplet diameter (Yi et al., 2021). For all the configurations (simulation and experiment as well as both volume fractions), $\sigma \approx 0.4$ can be used, which provides good results, as shown in Fig. 14. The value of σ decreases slightly with decreasing volume fraction.

The upper-limit log-normal (ULLN) distribution extends the log-normal distribution, incorporating an upper limit. This function is commonly used to model DSDs in applications where physical constraints limit droplet size (Babinsky and Sojka, 2002; Lekic et al., 1976; Solomon et al., 1985). It is defined by Eq. (10):

$$f_{\text{ULLN}}(d) = \frac{c_1 \cdot d_{\text{max}}}{\sqrt{\pi}d(d_{\text{max}} - d)} \exp\left(-c_1^2 \left[\ln\left(\frac{c_2 d}{d_{\text{max}} - d}\right)\right]^2\right) \quad (10)$$

In this equation, d_{max} represents the upper limit of the droplet diameter range. c_1 is defined as $1/(\sqrt{2} \ln \delta)$ and $c_2 = d_{\text{max}}/a$. Here, δ and a are fitting parameters. While δ is approximately 2.0 for all investigated configurations, a strongly differs between the simulation and experiment because of its dependency on d_{max} .

The Gamma distribution is another commonly used equation (Bremond and Villermaux, 2006; Hsieh et al., 2009; Villermaux, 2007; Willis and Tattelman, 1989; Yi et al., 2021). In this work, a modified formulation is used, which includes a characteristic diameter d_y . The function is independent of the number of droplets (in contrast to, e.g., Hsieh et al. (2009)). The distribution is given by

$$f_{\text{Gamma}}(d) = \frac{\gamma_2^{\gamma_1} \cdot d^{\gamma_1-1}}{\Gamma(\gamma_1) \cdot d_y^{\gamma_1}} \exp\left(-\frac{\gamma_2 \cdot d}{d_y}\right) \quad (11)$$

where $\Gamma(\gamma_1)$ is the Gamma function. The parameters γ_1 and γ_2 control the shape and scaling of the distribution. The parameter d_y is substituted by $d_{50,3}$ here. For the investigated cases, $\gamma_1 \approx \gamma_2$. This reduces the Gamma distribution to one fitting parameter. The results with this assumption can be found in Fig. 14. However, the values of

the fitting parameters depend on the configuration and increase with decreasing volume fraction. The parameters vary between $\gamma_1 \approx \gamma_2 \in [5.7, 8.8]$.

The beta distribution, as described by Watkins (2005), is commonly used to model data bounded between two limits and is written as

$$f_{\text{Beta}}(d) = \frac{(d - d_{\min})^{b_1 - 1} \cdot (d_{\max} - d)^{b_2 - 1}}{(d_{\max} - d_{\min})^{b_1 + b_2 - 1}} \cdot \frac{1}{\beta(b_1, b_2)} \quad (12)$$

with the beta function $\beta(b_1, b_2)$. The parameters b_1 and b_2 control the shape of the distribution. d_{\min} and d_{\max} represent the minimum and maximum diameters, respectively. Compared with the other distributions, this function is formulated in general terms and does not contain a representative diameter. The values of the fitting parameters differ slightly between the experimental and simulation results. Here, $\beta_1 \in [2.3, 3.4]$ and $\beta_2 \in [3.9, 5]$.

The Rosin-Rammler distribution is defined as (Babinsky and Sojka, 2002):

$$f_{\text{RR}}(d) = \frac{r_1}{d_{\text{rosin}}} \cdot \left(\frac{d}{d_{\text{rosin}}} \right)^{r_1 - 1} \exp \left(- \left(\frac{d}{d_{\text{rosin}}} \right)^{r_1} \right) \quad (13)$$

The parameter r_1 controls the shape of the distribution, and d_{rosin} is a representative diameter, which is $d_{50,3}$. In this work, r_1 increases with decreasing volume fraction. While r_1 is fitted to 2.7 and 3.0 for the experiment, the values for the simulation are $r_1 = 3.0$ and $r_1 = 3.25$. Using $r_1 = 3.0$ for all configurations provides similar results, which are shown in Fig. 14.

Additionally, a Nukiyama-Tanasawa (NT) distribution is considered (see, Babinsky and Sojka, 2002), which is modified within this work. The function was extended by a characteristic diameter d_{NT} and reduced by a fitting parameter. The NT function is based on the RR distribution. The formula can be written as

$$f_{\text{NT}}(d) = \frac{n_1}{d_{\text{NT}}} \left(\frac{d}{d_{\text{NT}}} \right)^{n_1 - 1} \exp \left(- \left(\frac{d}{d_{\text{NT}}} \right)^{n_2} \right) \quad (14)$$

The parameter n_1 controls the shape of the distribution, whereas n_2 determines the exponent of the exponential decay. Again, $d_{50,3}$ is used as d_{NT} . The formula is derived by considering the relationship between the droplet diameter and volume density. By modifying the original NT formula, this adaptation accounts for the specific requirements and characteristics of the data analyzed in this study. It offers an improved representation of the DSD within the given limits. Both fitting parameters increase with decreasing volume fraction. The values between the experimental and simulation results are quite similar and are between 2.3 and 3.3 for all configurations.

The root normal (RN) distribution is another function considered within this work. The RN distribution is given by Babinsky and Sojka (2002):

$$f_{\text{RN}}(d) = \frac{1}{\sqrt{2\pi d} \cdot 2R_1} \exp \left(-0.5 \left(\frac{\sqrt{d} - \sqrt{d_{\text{RN}}}}{R_1} \right)^2 \right) \quad (15)$$

where $d_{\text{RN}} = d_{50,3}$ and R_1 is a parameter governing the spread of the distribution. Here, in contrast to the other configurations, R_1 varies strongly between the simulation and experiment. The values for the experiment are 0.0014 for the high volume fraction and 0.0012 for the lower volume fraction. In contrast, the fitting parameters for the simulations are $R_1 \approx 0.1$.

Hyperbolic distributions (see, Babinsky and Sojka, 2002; Moradi et al., 2011) and the chi-square distribution (see, Lekic et al., 1976) have also been studied but have not been found to be suitable for volume distributions. Additionally, symmetric distribution functions such as the Gaussian distribution are also unsuitable for describing DSDs in this study.

Furthermore, mixed distribution models are proposed that combine the characteristics of different probability density functions. This approach allows to capture the features of both distributions and provides a more accurate description of the DSD in the analysis. The blended distribution is defined as

$$f_{\text{mix}}(d) = b \cdot f_1(d) + (1 - b) \cdot f_2(d) \quad (16)$$

In this equation, $f_{\text{mix}}(d)$ represents the volume distribution function of droplets as a function of d , the droplet diameter. The mixed distribution model combines the two functions by linearly interpolating them on the basis of the blending factor b . The best results were achieved by using a combination of the Gamma and NT distributions as well as the Gamma and ULLN distributions. For both, $b \approx 0.3$ is suitable.

The accuracy of statistical models can be assessed via various metrics. In this study, the following measures are employed: R^2 and the root mean square error (RMSE):

- R^2 is a statistical measure that indicates the proportion of the variance in the dependent variable that is predictable from the independent variables in a regression model. It ranges from 0 to 1, with a value of 1 indicating that the model explains all the variability of the dependent variable.
- The RMSE quantifies the average prediction error of a regression model. A lower RMSE value indicates a better fit between the model and the observed data, suggesting that the model's predictions are closer to the actual values.

By considering the R^2 and RMSE, it can be analyzed how well the models capture the observed data and make informed conclusions about their suitability for the considered cases. Only distributions with $RMSE < 0.02$ and $R^2 > 0.9$ were considered for the volume distributions. The results of the considered distributions are listed in Table 3.

The qualitative results of the distribution functions are displayed in Figs. 8, 9, and 10. The differences between the two volume distributions are small, indicating reasonable concordance for all the functions. However, the maximum of the on-injector distribution is slightly underestimated for all the functions except for Rosin–Rammler and NT.

In combination with the quantitative data in Table 3, a clearer picture emerges: excluding the mixed functions, the Gamma function best describes both the experimental and numerical distributions. The Rosin–Rammler function shows the poorest fit, with a significantly lower R^2 value. The other probability density functions in the middle range achieve similar error values. However, when comparing experiments and DNS, their order is different. For example, the beta distribution reaches the second-best values for the DNS, but the second-worst values are obtained for the on-injector data. The mixing of two different probability density functions delivers better concordance, depending on the chosen functions.

Overall, the agreement of the investigated functions depends on the number of fitting parameters since, in general, the shapes of their distributions are similar. A comparison of the Rosin–Rammler and the Nukiyama–Tanasawa

Table 3 Statistical fit evaluation for the volume distributions of the configurations. The distributions are sorted according to the R^2 and RMSE values

On-injector		
Function	R^2	RMSE
Rosin	0.91	0.0113
Beta	0.95	0.0090
NT	0.95	0.0086
LN	0.95	0.0084
ULLN	0.96	0.0076
RN	0.96	0.0074
Gamma	0.97	0.0064
Gamma-ULLN	0.97	0.0061
Gamma-NT	0.98	0.0060
Simulation		
Function	R^2	RMSE
Rosin	0.93	0.0110
LN	0.96	0.0088
RN	0.96	0.0087
NT	0.96	0.0087
ULLN	0.97	0.0074
Beta	0.97	0.0074
Gamma	0.98	0.0066
Gamma-NT	0.98	0.0062
Gamma-ULLN	0.98	0.0061

functions clarifies this. Both equations differ only in terms of the number of fitting parameters: the RR equation has

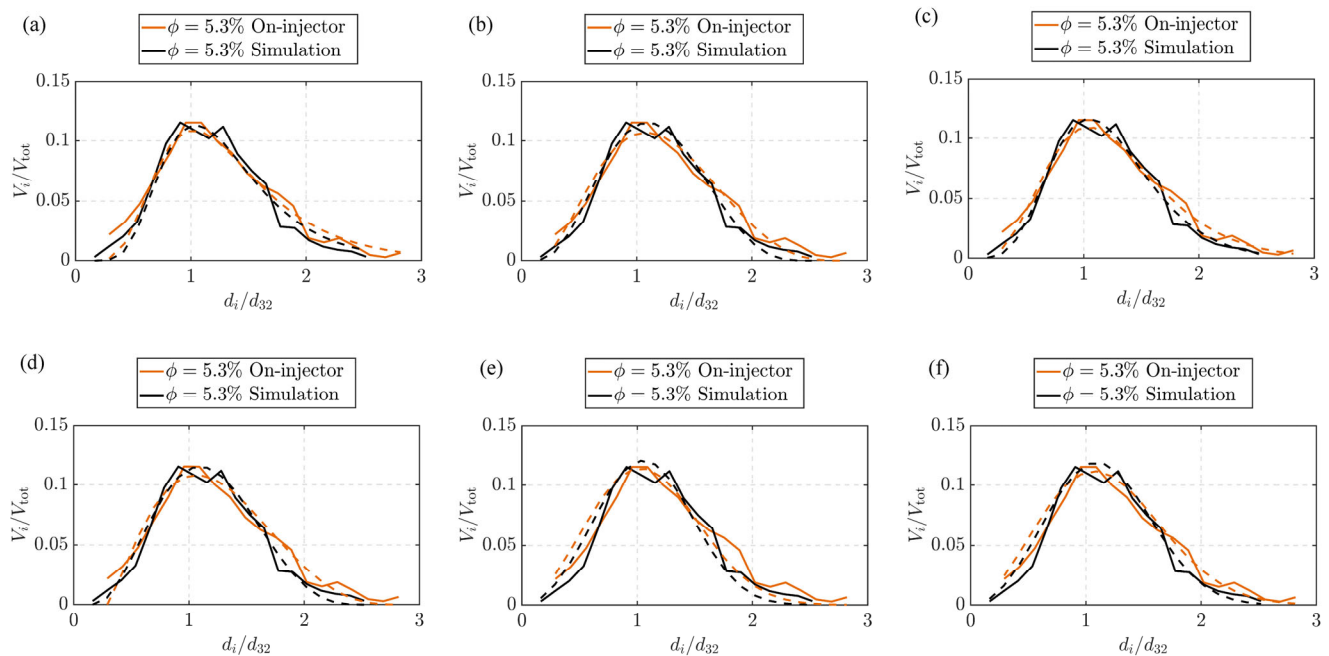


Fig. 8 PDFs of the volume distributions: (a) LN, (b) ULLN, (c) gamma, (d) beta, (e) Rosin–Rammler, (f) NT.

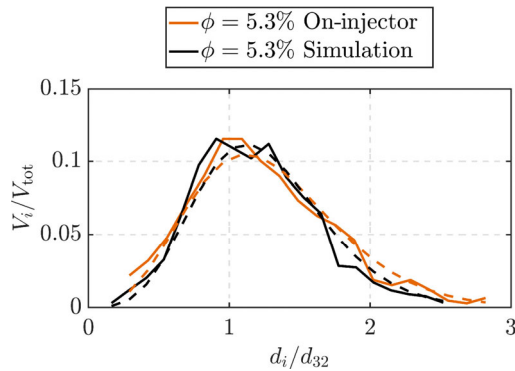


Fig. 9 PDFs of the volume distributions with the NT function.

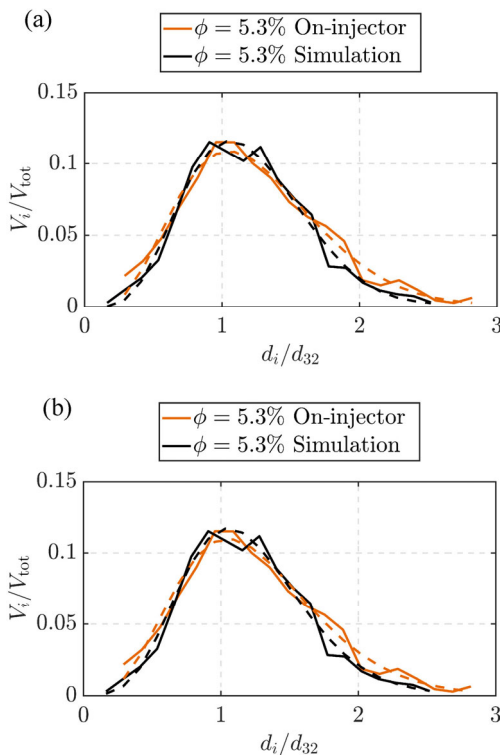


Fig. 10 PDFs of the volume distributions with fitted mixed functions: (a) gamma-Ulln and (b) gamma-NT.

one fitting parameter, and the NT equation has two fitting parameters, resulting in significantly better error values. Blending several functions results in the lowest error but obviously increases complexity and the number of fitting parameters. The goal of the investigated distributions is to predict droplet size distributions with a measured or calculated characteristic diameter. Thus, knowledge of the fitting parameters, which should be independent of the configuration, is obligatory. The best results were obtained via the log-normal function. Independent of the configuration, the fitting parameter can be assumed to be 0.4 for volume fractions in the investigated range and when $d_{50,3}$ is used as the characteristic diameter. Additionally, the fitting parameter of the Rosin–Rammler function can be considered to be

$r_1 \approx 3.0$. However, this function provides a poorer fit than the LN distribution. The findings for the Gamma distribution should be investigated in more detail because this distribution can be reduced to one fitting parameter for the investigated cases. Moreover, the second fitting parameter of the ULLN distribution can be assumed to be 2.0 for the examined experiments and simulations. However, the other fitting parameters strongly depend on d_{\max} and thus vary with different physical parameters.

6 Conclusions

In this work, experimental and numerical studies are combined to expand the knowledge of the physics of water-in-gasoline emulsions. Two different approaches for producing such emulsions were presented: the on-injector system and the single-HPP system, which differ in terms of process layout and emulsification itself. Direct numerical simulations are conducted under idealized homogeneous isotropic turbulence conditions. Because it was not possible to assess the experimental flow conditions fully, some assumptions and simplifications had to be made. Nevertheless, the turbulent conditions in the simulation are comparable to those in the experiments. In this work, the focus is on the droplet size distributions. The main findings can be summarized as follows.

The volume distributions obtained in the on-injector system can be successfully described by the idealized DNS. Moreover, a similar behavior can be identified when the dispersed volume fraction is increased. Owing to the greater number of droplets, coalescence is promoted, which ultimately leads to distributions with an increased quantity of larger droplets. Thus, the simulation effectively represents the flow conditions for emulsification in the on-injector system.

Compared with the single-HPP experiments, more differences were identified. Although the same trend of larger droplets with increased water volume fraction is observed, the distributions differ significantly. The reason is most likely the design of the experimental process. Following the homogenization of the emulsion in the high-pressure pump, coalescence occurring in the components downstream influences the distributions. Consequently, this leads to a system behavior that cannot be adequately predicted by the DNS with the chosen boundary conditions. Comparing DNS results with the emulsion before the rail would be insightful, but only qualitative experimental results are available at this point because the droplets are too small for the detection software. A possibility would be to adapt the simulation by allowing a certain amount of segregation and detecting the droplets afterwards.

Probability density functions are useful for defining particulate distributions with a small number of parameters. In this work, suitable functions that can describe the experimental and simulated droplet size distributions were identified. The gamma distribution provides the best fit, and it was possible to reduce the number of fitting parameters from two to one. However, the remaining parameter was dependent on the respective distribution. The log-normal distribution fitting parameter, on the other hand, was largely invariant across the configurations studied. Although the quantitative evaluation of the fit shows slightly poorer values, the log-normal function is the best compromise between accuracy and simplicity for the investigated cases. Therefore, when $d_{50,3}$ is measurable or predictable by simple models, it can be used for similar applications to predict DSDs. To make more reliable statements about the influence of physical factors on the fitting parameters, one would need a broader database of measured and simulated distributions.

Overall, the results illustrate the possibility of combining industrial process experiments with simplified direct numerical simulations to gain more insight into the physics of emulsification. Although simulations and experiments are limited by their own constraints, such as optical accessibility or computational resources, a combination of

both allows for an expansion of knowledge. Thus, trends in droplet size distribution can likely be predicted beyond the capabilities of experimental measurements, e.g., by providing additional phase and velocity information in three dimensions or quantitative information on segregation behavior.

Future work will focus on expanding the knowledge on segregation processes by combining DNS and experimental data. Moreover, regarding the practical application of GWDI, emulsion spray breakup is currently under investigation.

Appendix 1 Statistically steady state of DNS

The normalized interface area is plotted against the normalized time in Fig. 11(a). A completely segregated state, defined as $A_\infty = L^2 = (2\pi)^2$, is used as a reference for the interface area. After $t/\tau = 3$ (τ is the eddy turnover time), both configurations reach the steady state.

This observation is further supported by Fig. 11(b), which shows the rate of change in the interface area, denoted as \dot{A} , plotted against the normalized time for the configuration where $\phi = 5.3\%$. After reaching $t/\tau = 3$, the rate of change \dot{A} fluctuates around zero.

Additionally, as expected, the interface area significantly increases with increasing volume fraction. Figure 12 illustrates the considered cases at the HIT.

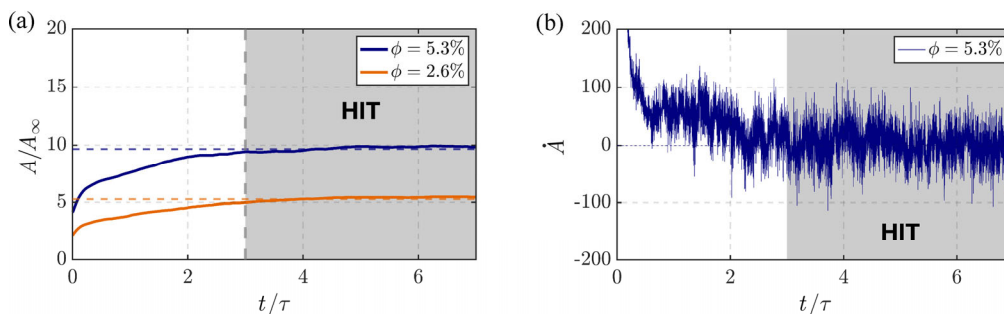


Fig. 11 Normalized temporal evolution of (a) the interface area ratio A/A_∞ for all configurations and (b) the rate of change in the interface area \dot{A} for $\phi = 5.3\%$. The steady state is reached at $t/\tau = 3$ (colored gray). The horizontal dashed lines in (a) indicate the average values of A/A_∞ in the steady state.

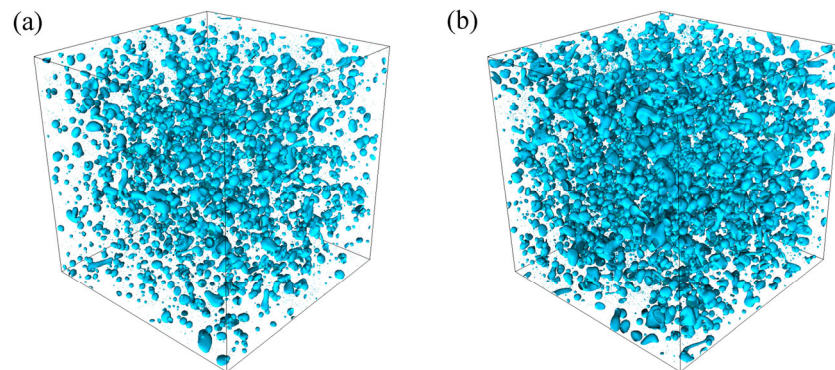


Fig. 12 Illustration of the different configurations in a statistically steady state at time $t/\tau \approx 6$: (a) $\phi = 2.6\%$ and (b) $\phi = 5.3\%$.

Appendix 2 Influence of TKE

Figure 13 compares the results between two different simulations with modified TKE. The TKE $k = 2.0 \text{ m}^2/\text{s}^2$, which was clearly too high for comparison with the experimental data, was compared with the TKE $k = 0.5 \text{ m}^2/\text{s}^2$. A detailed analysis of the influence of the turbulence intensity on the characteristics of emulsions with similar configurations was carried out by Begemann et al. (2022). The curves clearly shift with increasing TKE. The number of smaller droplets increases with increasing Reynolds and Weber numbers, leading to a more pronounced dominance of breakup processes. Consequently, larger droplets become less frequent.

Another notable finding is the effect on the SMD. As the SMD changes with the presence of smaller droplets, resulting in an increased interface area ($d_{32} \propto 1/A$, see Eq. (8)), normalization with d_{32} ensures that the curves are centered but do not match. A fourfold greater TKE leads to an earlier rise and a greater peak. Additionally, the curves at higher TKE are smoother, reflecting the increased number of droplets and, consequently, more statistically reliable results.

On the basis of the experimental measurements, the TKE in the simulation was set to $k = 0.5 \text{ m}^2/\text{s}^2$ to ensure good comparability with the flow parameters in the experimental system.

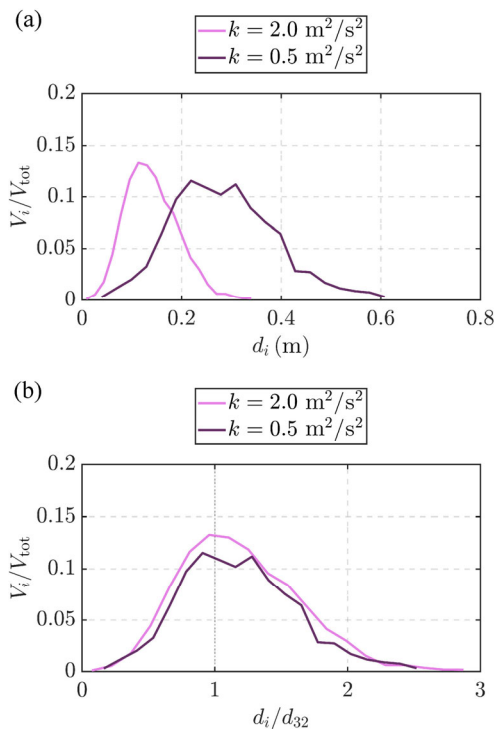


Fig. 13 Comparison of volume distributions between simulations with TKE $k = 2.0 \text{ m}^2/\text{s}^2$ and TKE $k = 0.5 \text{ m}^2/\text{s}^2$. The plot (b) is normalized with the SMD.

Appendix 3 Fitting parameters of the distribution functions

Table 4 provides an overview of the fitting parameters of the distribution function for each investigated configuration. In Fig. 14, the log-normal, Rosin–Rammler, and gamma functions are plotted with generalized fitting factors and are compared with the numerical and experimental data. The assumptions for the LN and gamma distributions are

Table 4 Calculated fitting parameters for each distribution function depending on the investigated configurations

	On-injector 5.3%	On-injector 2.6%	Simulation 5.3%	Simulation 2.6%
LN	$\sigma = 0.42$	$\sigma = 0.38$	$\sigma = 0.39$	$\sigma = 0.37$
ULLN	$a = 7 \times 10^{-5}$	$a = 6.4 \times 10^{-5}$	$a = 0.5$	$a = 0.45$
Gamma	$\gamma_1 = 5.8$ $\gamma_2 = 5.7$	$\gamma_1 = 7.5$ $\gamma_2 = 7.4$	$\gamma_1 = 7.3$ $\gamma_2 = 7.3$	$\gamma_1 = 8.8$ $\gamma_2 = 8.7$
Beta	$\beta_1 = 2.3$ $\beta_2 = 4.0$	$\beta_1 = 2.8$ $\beta_2 = 5.0$	$\beta_1 = 3.3$ $\beta_2 = 4.5$	$\beta_1 = 3.4$ $\beta_2 = 3.9$
Rosin-Rammler	$r_1 = 2.7$	$r_1 = 3.0$	$r_1 = 3.0$	$r_1 = 3.3$
NT	$n_1 = 2.7$ $n_2 = 2.3$	$n_1 = 3.1$ $n_2 = 2.7$	$n_1 = 3.0$ $n_2 = 2.7$	$n_1 = 3.3$ $n_2 = 2.9$
RN	$R_1 = 0.0014$	$R_1 = 0.0012$	$R_1 = 0.1$	$R_1 = 0.09$

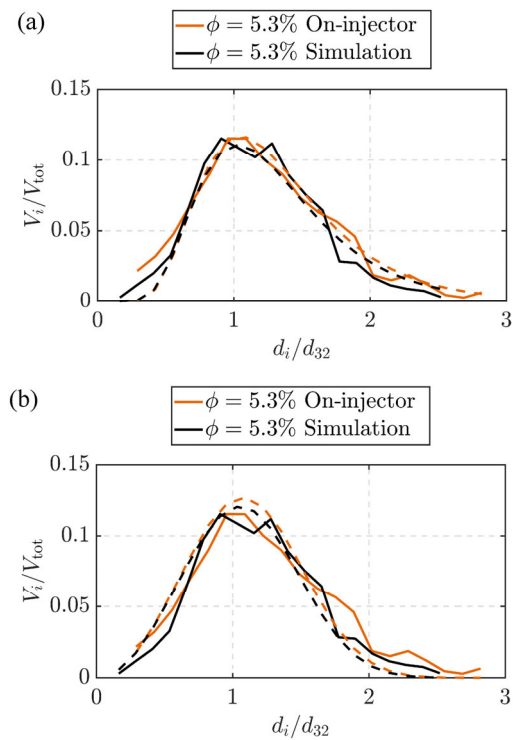


Fig. 14 PDFs of the volume distributions with generalized fitting parameters: (a) LN with $\sigma = 0.4$, (b) Rosin–Rammler with $r_1 = 3.0$, and (c) gamma with $\gamma_1 = \gamma_2$.

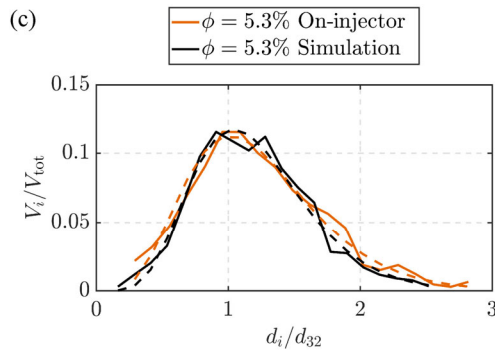


Fig. 14 (Continued)

similar to the results in Section 5.3, whereas the Rosin-Rammler function shows some deviations. Additionally, the fitting parameters of the experiment and DNS react similarly to a change in the volume fraction. For the log-normal distribution, a lower volume fraction leads to a decreased fitting parameter σ , which indicates that the distributions become narrower at lower volume fractions. This underlines the observations made in Section 5.2.

Funding note

Open Access funding enabled and organized by Projekt DEAL.

Acknowledgements

This project received funding from *dtec.bw* (Digitalization and Technology Research Center of the Bundeswehr) under the project MORE, which is gratefully acknowledged. *dtec.bw* is funded by the European Union (NextGenerationEU). Furthermore, the authors thank the Gauss Centre for Supercomputing e.V. (www.gauss-centre.eu) for funding this project by providing computing time on the GCS Supercomputer SuperMUC-NG at the Leibniz Supercomputing Centre (www.lrz.de). The experiments were funded by the Rhineland-Palatinate “Large-scale Equipment” funding program.

Declaration of competing interest

The authors have no competing interests to declare that are relevant to the content of this article.

References

Akehurst, S., Giles, K., Howson, S., Lewis, A., Yuan, H., Harris, J., Fowler, G., Geddes, J. 2019. An experimental study of water injection in a downsized, highly boosted direct injection spark ignition engine. In: Proceedings of the 28th Aachen Colloquium Automobile and Engine Technology, 1029–1058.

- Angardi, V., Etehad, A., Yücel, Ö. 2022. Critical review of emulsion stability and characterization techniques in oil processing. *Journal of Energy Resources Technology*, 144: 040801.
- Angeli, P., Hewitt, G. F. 2000. Drop size distributions in horizontal oil-water dispersed flows. *Chemical Engineering Science*, 55: 3133–3143.
- Aniszewski, W., Arrufat, T.1, Cialesi-Esposito, M., Dabiri, S., Fuster, D., Ling, Y., Lu, J., Malan, L., Pal, S., Scardovelli, R. et al. 2021. PArallel, robust, interface simulator (PARIS). *Computer Physics Communications*, 263: 107849.
- Babinsky, E., Sojka, P. E. 2002. Modeling drop size distributions. *Progress in Energy and Combustion Science*, 28: 303–329.
- Begemann, A., Trummel, T., Trautner, E., Hasslberger, J., Klein, M. 2022. Effect of turbulence intensity and surface tension on the emulsification process and its stationary state—A numerical study. *The Canadian Journal of Chemical Engineering*, 100: 3548–3561.
- Blau, B., Heinrich, C., Klein, M. 2022. Gasoline water direct injection (GWDI): Optical investigations on fuel-water emulsions in the injection system. In: *31st Aachen Colloquium Sustainable Mobility 2022*. Aachener Kolloquium Fahrzeug- und Motorentechnik GbR, Paper No. Pos01.
- Blau, B., Heinrich, C., Klein, M. 2023. Droplet size analysis of gasoline-water emulsions in the high-pressure injection system – Influence of system design and operating parameters on emulsion quality. In: *12. Tagung Einspritzung und Kraftstoffe*. Tschöke, H., Reiser, C., Stenzel, K., Eds. Forschungszentrum für Verbrennungsmotoren und Thermodynamik Rostock GmbH, 70–82.
- Boxall, J. A., Koh, C. A., Sloan, E. D., Sum, A. K., Wu, D. T. 2010. Measurement and calibration of droplet size distributions in water-in-oil emulsions by particle video microscope and a focused beam reflectance method. *Industrial & Engineering Chemistry Research*, 49: 1412–1418.
- Brackbill, J. U., Kothe, D. B., Zemach, C. 1992. A continuum method for modeling surface tension. *Journal of Computational Physics*, 100: 335–354.
- Bremond, N., Villiermaux, E. 2006. Atomization by jet impact. *Journal of Fluid Mechanics*, 549: 273.
- Chan, W. H. R., Dodd, M. S., Johnson, P. L., Moin, P. 2021. Identifying and tracking bubbles and drops in simulations: A toolbox for obtaining sizes, lineages, and breakup and coalescence statistics. *Journal of Computational Physics*, 432: 110156.
- Cialesi-Esposito, M., Chibbaro, S., Brandt, L. 2023. The interaction of droplet dynamics and turbulence cascade. *Communications Physics*, 6: 5.
- Cialesi-Esposito, M., Rosti, M. E., Chibbaro, S., Brandt, L. 2022. Modulation of homogeneous and isotropic turbulence in emulsions. *Journal of Fluid Mechanics*, 940: A19.
- Deberne, C., Chéron, V., Poux, A., Brändle de Motta, J. C. 2024. Breakup prediction of oscillating droplets under turbulent flow. *International Journal of Multiphase Flow*, 173: 104731.
- Durst, B., Landerl, C., Poggel, J., Schwarz, C., Kleczka, W., Hußmann, B. 2017. BMW Wassereinspritzung: Erste Erfahrungen und künftige

- Potenziale. In: 38. *Internationales Wiener Motorensymposium*. Lenz, H. P., Ed. Verkehrstechnik Fahrzeugtechnik, 63–79.
- Galinat, S., Torres, L. G., Masbernat, O., Guiraud, P., Risso, F., Dalmazzone, C., Noik, C. 2007. Breakup of a drop in a liquid–liquid pipe flow through an orifice. *AIChE Journal*, 53: 56–68.
- Gern, M. S. 2021. *Experimentelle Entwicklung einer Einspritzstrategie für Ottomotoren mit Wassereinspritzung*. Springer Vieweg Wiesbaden.
- Håkansson, A., Cialesi-Esposito, M., Nilsson, L., Brandt, L. 2022. A criterion for when an emulsion drop undergoing turbulent deformation has reached a critically deformed state. *Colloids and Surfaces A: Physicochemical and Engineering Aspects*, 648: 129213.
- Heinrich, C., Dörksen, H., Esch, A., Krämer, K. 2018. Gasoline water direct injection (GWDI) as a key feature for future gasoline engines. In: *Knocking in Gasoline Engines*. Günther, M., Sens, M., Eds. Springer Cham, 322–337.
- Heinrich, C., Dörksen, H., Tölkes, E., Esch, A. 2017. Direkte Benzin-Wasser-Einspritzung: CO₂-Potentiale und technische Anforderungen. In: 10. *Tagung Diesel- und Benzindirekteinspritzung 2016*. Tschöke, H., Marohn, R., Eds. Springer Vieweg, Wiesbaden, 363–379.
- Hermann, I., Glahn, C., Kluin, M., Paroll, M. 2017. Thermodynamisches Potential der Wassereinspritzung für den Ottomotor. In: *Der Arbeitsprozess des Verbrennungsmotors*. IVT-Mitteilungen, Verlag der Technischen Universität Graz, Graz.
- Hermann, I., Glahn, C., Kluin, M., Paroll, M., Gumprich, W. 2018. Water injection for gasoline engines - quo vadis? In: *Knocking in Gasoline Engines*. Günther, M., Sens, M., Eds. Springer Cham, 299–321.
- Hesketh, R. P., Fraser Russell, T. W., Etchells, A. W. 1987. Bubble size in horizontal pipelines. *AIChE Journal*, 33: 663–667.
- Hinze, J. O. 1955. Fundamentals of the hydrodynamic mechanism of splitting in dispersion processes. *AIChE Journal*, 1: 289–295.
- Hsieh, W. C., Jonsson, H., Wang, L. P., Buzorius, G., Flagan, R. C., Seinfeld, J. H., Nenes, A. 2009. On the representation of droplet coalescence and autoconversion: Evaluation using ambient cloud droplet size distributions. *Journal of Geophysical Research: Atmospheres*, 114: D07201.
- Krzeczek, O., Trummel, T., Trautner, E., Klein, M. 2023. Effect of the density ratio on emulsions and their segregation: A direct numerical simulation study. *Energies*, 16: 3160.
- Lekic, A., Bajramovic, R., Ford, J. D. 1976. Droplet size distribution: An improved method for fitting experimental data. *The Canadian Journal of Chemical Engineering*, 54: 399–402.
- Ling, Y., Zaleski, S., Scardovelli, R. 2015. Multiscale simulation of atomization with small droplets represented by a Lagrangian point-particle model. *International Journal of Multiphase Flow*, 76: 122–143.
- Maaß, S., Kraume, M. 2012. Determination of breakage rates using single drop experiments. *Chemical Engineering Science*, 70: 146–164.
- Maaß, S., Paul, N., Kraume, M. 2012. Influence of the dispersed phase fraction on experimental and predicted drop size distributions in breakage dominated stirred systems. *Chemical Engineering Science*, 76: 140–153.
- Moradi, M., Alvarado, V., Huzurbazar, S. 2011. Effect of salinity on water-in-crude oil emulsion: Evaluation through drop-size distribution proxy. *Energy & Fuels*, 25: 260–268.
- Mukherjee, S., Safdari, A., Shardt, O., Kenjereš, S., Van den Akker, H. E. A. 2019. Droplet–turbulence interactions and quasi-equilibrium dynamics in turbulent emulsions. *Journal of Fluid Mechanics*, 878: 221–276.
- Mukundan, A. A., Tretola, G., Ménard, T., Herrmann, M., Navarro-Martinez, S., Vogiatzaki, K., de Motta, J. C. B., Berlemont, A. 2021. DNS and LES of primary atomization of turbulent liquid jet injection into a gaseous crossflow environment. *Proceedings of the Combustion Institute*, 38: 3233–3241.
- Olad, P., Innings, F., Cialesi-Esposito, M., Brandt, L., Håkansson, A. 2023. Comparison of turbulent drop breakup in an emulsification device and homogeneous isotropic turbulence: Insights from numerical experiments. *Colloids and Surfaces A: Physicochemical and Engineering Aspects*, 657: 130569.
- Pacek, A. W., Man, C. C., Nienow, A. W. 1998. On the Sauter mean diameter and size distributions in turbulent liquid/liquid dispersions in a stirred vessel. *Chemical Engineering Science*, 53: 2005–2011.
- Panão, M. R. O. 2023. Why drop size distributions in sprays fit the lognormal. *Physics of Fluids*, 35: 011701.
- Perlekar, P., Biferale, L., Sbragaglia, M., Srivastava, S., Toschi, F. 2012. Droplet size distribution in homogeneous isotropic turbulence. *Physics of Fluids*, 24: 065101.
- Peters, B. D., Stebar, R. F. 1976. Water-gasoline fuels-their effect on spark ignition engine emissions and performance. *SAE Technical Paper*, 760547.
- Plasencia, J., Inkson, N., Nydal, O. J. 2022. Research on the viscosity of stabilized emulsions in different pipe diameters using pressure drop and phase inversion. *Experimental and Computational Multiphase Flow*, 4: 241–263.
- Pope, S. B. 2001. Turbulent flows. *Measurement Science and Technology*, 12: 2020–2021.
- Popinet, S. 2009. An accurate adaptive solver for surface-tension-driven interfacial flows. *Journal of Computational Physics*, 228: 5838–5866.
- Rayner, M., Dejmek, P. 2015. *Engineering Aspects of Food Emulsification and Homogenization*. Boca Raton: CRC Press.
- Rohit, A., Satpathy, S., Choi, J., Hoard, J., Surnilla, G., Hakeem, M. 2017. Literature survey of water injection benefits on boosted spark ignited engines. *SAE Technical Paper*, 2017-01-0658.
- Rosales, C., Meneveau, C. 2005. Linear forcing in numerical simulations of isotropic turbulence: Physical space implementations and convergence properties. *Physics of Fluids*, 17: 095106.
- Sazonov, V., Rottengruber, H., Dragomirov, P. 2019. Untersuchung der Benzin-Wasser-Emulsion Direkteinspritzung zur Effizienzsteigerung von Ottomotoren. In: 11. *Tagung Einspritzung und Kraftstoffe 2018*. Tschöke, H., Marohn, R., Eds. Springer Vieweg, Wiesbaden, 515–542.
- Schümann, H., Tutkun, M., Nydal, O. J. 2016. Experimental study of

- dispersed oil-water flow in a horizontal pipe with enhanced inlet mixing, Part 2: *in situ* droplet measurements. *Journal of Petroleum Science and Engineering*, 145: 753–762.
- Simmons, M. J. H. 2000. Comparison of laser-based drop-size measurement techniques and their application to dispersed liquid-liquid pipe flow. *Optical Engineering*, 39: 505.
- Skartlien, R., Sollum, E., Schumann, H. 2013. Droplet size distributions in turbulent emulsions: Breakup criteria and surfactant effects from direct numerical simulations. *The Journal of Chemical Physics*, 139: 174901.
- Sleicher, C. A. 1962. Maximum stable drop size in turbulent flow. *AIChE Journal*, 8: 471–477.
- Solomon, K. H., Kincaid, D. C., Bezdek, J. C. 1985. Drop size distributions for irrigation spray nozzles. *Transactions of the ASAE*, 28: 1966–1974.
- Spernath, A., Aserin, A. 2006. Microemulsions as carriers for drugs and nutraceuticals. *Advances in Colloid and Interface Science*, 128: 47–64.
- Stang, M., Schuchmann, H., Schubert, H. 2001. Emulsification in high-pressure homogenizers. *Engineering in Life Sciences*, 1: 151–157.
- Trautner, E., Hasslberger, J., Ketterl, S., Klein, M. 2023. Primary atomization of liquid jets: Identification and investigation of droplets at the instant of their formation using direct numerical simulation. *International Journal of Multiphase Flow*, 160: 104360.
- Trummler, T., Begemann, A., Trautner, E., Klein, M. 2022. Numerical investigation of the segregation of turbulent emulsions. *Physics of Fluids*, 34: 113324.
- Villermaux, E. 2007. Fragmentation. *Annual Review of Fluid Mechanics*, 39: 419–446.
- Watkins, A. P. 2005. The application of gamma and beta number size distributions to the modelling of sprays. In: Proceedings of the 20th ILASS, Orlean, France, 4–7.
- Willis, P. T., Tattelman, P. 1989. Drop-size distributions associated with intense rainfall. *Journal of Applied Meteorology*, 28: 3–15.
- Yi L., Toschi, F., Sun C. 2021. Global and local statistics in turbulent emulsions. *Journal of Fluid Mechanics*, 912: A13.
- Open Access** This article is licensed under a Creative Commons Attribution 4.0 International License, which permits use, sharing, adaptation, distribution and reproduction in any medium or format, as long as you give appropriate credit to the original author(s) and the source, provide a link to the Creative Commons license, and indicate if changes were made.
- The images or other third party material in this article are included in the article's Creative Commons license, unless indicated otherwise in a credit line to the material. If material is not included in the article's Creative Commons license and your intended use is not permitted by statutory regulation or exceeds the permitted use, you will need to obtain permission directly from the copyright holder.
- To view a copy of this license, visit <http://creativecommons.org/licenses/by/4.0/>.